UNIVERSITY OF OKLAHOMA GRADUATE COLLEGE

COMPUTATIONAL ASSESSMENT OF KEY PROPERTIES IN CoNiRu ALLOYS USING ATOMISTIC SIMULATIONS

A THESIS

SUBMITTED TO THE GRADUATE FACULTY

in partial fulfillment of the requirements for the
Degree of
MASTER OF SCIENCE

By THU NGUYEN

Norman, Oklahoma
2025

COMPUTATIONAL ASSESSMENT OF KEY PROPERTIES IN CoNiRu ALLOYS USING ATOMIC SIMULATIONS

A THESIS APPROVED FOR THE
SCHOOL OF AEROSPACE AND MECHANICAL ENGINEERING

BY THE COMMITTEEE CONSISTING OF

Dr. Iman Ghamarian, Chair

Dr. Shuozhi Xu, Co-Chair

Dr. Hanping Ding

Acknowledgements

First, I would like to thank my Godfather, Loi Nguyen, who came to America by boat and, despite the challenges of being a first-generation immigrant, earned a Bachelor's degree in Electrical Engineering from Oklahoma State University. He later sponsored my family and the families of three of his siblings, providing us with housing, food, and early career guidance that helped us all become self-sufficient in a new country.

To my parents, Toan Nguyen and Yen Huynh—thank you for making the difficult decision to leave Vietnam and giving me the life I have today. Though they had little, they always ensured we had shelter, food, and support. Their generosity included the gift of a new car to recognize my academic achievement in high school. To my mother especially—thank you for giving up your education, career, and family ties to build a better future for me and my younger brother.

I would also like to thank Dr. Iman Ghamarian for graciously welcoming me into his lab as a graduate research assistant during a time of uncertainty in my life. His support, honesty, and perspective offered me direction when I needed it most. I am equally thankful to Dr. Shuozhi Xu, whose passion and energy continue to inspire me. Every discussion with him has always been so full of passion, heart, and creativity. It has pushed me to grow as a scientist, engineer, and innovator and being around him has truly inspired me to pursue more. I am sincerely appreciative of both professors for their guidance and belief in me—I would not have rediscovered my confidence and passion without the both of you.

Finally, my last appreciation is extended to Dr. Hanping Ding, Anvesh Nathani, and Subah Mubassira for their consistent patience and readiness to provide support. Their guidance made a meaningful difference throughout the course of this research. I wish them nothing but the best in their continued pursuit of knowledge.

Table of Contents

List of Figure

List of Tables

Abstract

Reliable prediction of material behavior at the atomic scale is critical for the design, improvement, and development of high-performance structural alloys. Among them, the CoNiRu-based alloy has emerged as a promising candidate to many applications in aerospace, nuclear energy, and high-temperature manufacturing due to its high tolerance to mechanical loading, thermal stability, and potential for use in extreme environments. In this study, the CoNiRu ternary alloy system is systematically evaluated using atomistic simulations implemented in Large-scale Atomic/Molecular Massively Parallel Simulator (LAMMPS), where a universal machine learning interatomic potential (uMLIP) model is benchmarked against density functional theory (DFT) results. The uMLIP is assessed for its ability to predict lattice parameters and elastic constants in face-centered cubic (FCC) and hexagonal close-packed (HCP) structures at 0 K and 300 K, as well as generalized stacking fault energies (GSFE) in FCC and HCP structures at 0 K. The findings of this work offer critical insight into whether uMLIP can accurately approximate key mechanical and structural properties of CoNiRu alloys when compared to DFT results. The capabilities and limitations of uMLIP for modeling multi-component alloy systems will be tested, with implications for accelerated alloy design and deployment in advanced engineering applications. Gathering atomic simulation data using uMLIP proves to be promising and resource-efficient when juxtaposed with DFT method of data collection.

Chapter 1: Introduction

1.1 Motivation and Relevance of CoNiRu

The development of testing high-performance structural alloys has been a cornerstone of advancement for modern engineering solutions, particularly in applications involving extreme environments such as aerospace propulsion, nuclear reactors, and high-temperature manufacturing [1] [2]. In these domains, materials must exhibit exceptional mechanical strength, thermal stability, and resistance to deformation mechanisms such as dislocation slip and creep. The ability to predict and tailor material properties at the atomic scale is therefore essential to accelerate alloy design and reduce reliance on costly experimental trial-and-error approaches.

Among emerging high-performance structural alloy candidates, the CoNiRu ternary alloy system has attracted significant attention due to its promising mechanical and thermal characteristics. As a multi-component alloy composed of transition metals, CoNiRu offers the potential for enhanced strength, phase stability, and defect resistance through compositional tuning and chemical ordering [3]. Despite its potential, however, a comprehensive understanding of its fundamental mechanical behavior remains limited. Reliable modeling tools are needed to characterize critical material parameters that govern performance under service conditions.

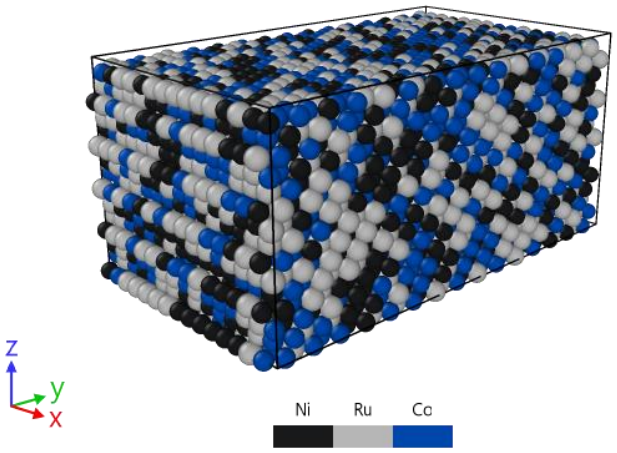

Figure 1: Atomic Model of Equimolar FCC CoNiRu

Reliable prediction of material properties at the atomic scale plays a central role in accelerating alloy design. First-principles methods such as DFT offer high accuracy in calculating structural and mechanical properties; however, their high computational cost limits their applicability to small systems and a narrow range of compositions [4][5]. To overcome these limitations, recent efforts have turned to machine learning data-driven trained modeling, particularly the use of uMLIP, which aims to reproduce the accuracy of DFT while enabling simulations at significantly larger scales and lower computational cost.

In this study, a uMLIP model is integrated within the LAMMPS framework to investigate the key properties of CoNiRu-based alloys. Simulations are performed on five systems: CoNiRu in FCC and HCP structures, Co_2Ni_2Ru (FCC), $CoNiRu_2$ (HCP), and pure Ni (FCC). For each structure, key material descriptors—including lattice parameters and elastic constants—are calculated at 0 K and 300 K, and GSFE are evaluated at 0 K. To validate the predictive performance of the uMLIP, the results are benchmarked against DFT-based simulations. The resulting comparison provides a baseline for assessing the accuracy of the uMLIP approach in modeling multi-component alloy systems. Through this dual-framework evaluation, the study aims to offer insights into the applicability of universal MLIPs for structural alloy design and their role in bridging the gap between computational efficiency and predictive fidelity.

1.2 Challenges in Modern Day Predictive Modeling

The accurate prediction of key behavior in complex alloy systems such as the three-part CoNiRu alloy presents a longstanding challenge in materials science. As alloy compositions increase in complexity, so too do the interatomic interactions, thermodynamic behavior, and defect dynamics that govern macroscopic performance [9] [10]. Traditional alloy development, based on empirical testing and thermodynamic approximations, is limited by both the high cost and high testing time associated with experimental trial-and-error [11] [12]. Thus, the development of computational modeling for atomic simulations has become a critical tool for understanding and optimizing material behavior.

In multi-component systems such as CoNiRu alloys, predictive modeling is complicated by several factors. First, the presence of three or more principal elements introduces a high degree of chemical disorder, which affects atomic-scale interactions and renders the use of simplistic pairwise potentials, the measure of interactions between two objects located in

Euclidean space, insufficient. Furthermore, these alloys may adopt multiple stable or metastable phases—such as FCC and HCP—whose stability depends sensitively on temperature, local chemical ordering, and composition [13] [14][15]. As such, phase-specific properties such as lattice parameters, elastic constants, and generalized stacking fault energies must be evaluated across a range of structural configurations and thermodynamic conditions.

1.3 From Classical Potentials to Machine Learning Potentials

Historically, atomistic simulations have relied on classical interatomic potentials to model the interactions between atoms in solid-state systems [16]. These models, such as the Lennard-Jones potential, Embedded Atom Method, and Modified Embedded Atom Method, are built upon analytical functional forms with parameters fitted to experimental measurements or limited quantum mechanical calculations. While effective for simple metallic systems and select alloy compositions, classical potentials suffer from limited flexibility and accuracy when extended to complex, chemically diverse systems [17].

One critical limitation of classical potential lies in their inability to capture the many-body nature of interatomic interactions with high fidelity. Their functional forms are often rigid, and their transferability is constrained to the specific configurations or element combinations on which they were parameterized. In the context of multi-component systems like CoNiRu, this restricts their predictive power, especially when modeling off-equiatomic compositions, multiple crystal structures, or temperature-dependent behavior.

Machine learning interatomic potential has emerged as a powerful alternative that overcomes many of these limitations. Unlike classical models, MLIPs are trained directly on data, such as validated DFT-calculated energies, forces, and stresses, using non-linear statistical or neural network-based regression techniques [18][19]. This data-driven approach enables the MLIP to implicitly capture complex bonding characteristics and subtle variations in atomic environments that would otherwise be neglected or oversimplified in classical models.

1.4 Objective of the Study

The central objective of this study is to evaluate the effectiveness of a uMLIP in predicting key structural and mechanical properties of CoNiRu-based alloys. Specifically, the research investigates whether the uMLIP—trained on a diverse database of elemental and

compound systems—can serve as a computationally efficient and accurate alternative to DFT in modeling chemically complex alloys. This objective is pursued through the application of atomistic simulations using the LAMMPS software package, in which the uMLIP model is implemented. A systematic series of simulations is conducted on the CoNiRu alloy system and related compositions to quantify the uMLIP's performance. The focus lies on calculating three classes of material properties: lattice parameters, elastic constants, and GSFE. These properties are essential for understanding atomic-scale behavior such as crystal stability, deformation resistance, and dislocation motion.

To assess predictive reliability, uMLIP-derived results are benchmarked against published and unpublished DFT data across multiple compositions, crystal structures, and temperature conditions. The alloys considered include equiatomic CoNiRu in both FCC and HCP phases, as well as non-equiatomic compositions (Co_2Ni_2Ru and $CoNiRu_2$), and pure Ni. Simulations for lattice parameter and elastic constant are performed at 0 K and 300 K to evaluate the model's performance under static and thermally relaxed conditions. Through this investigation, the study seeks to contribute to the broader effort of accelerating material discovery by validating machine learning frameworks capable of delivering near-DFT accuracy at a fraction of the computational cost.

Chapter 2: Modeling Approach

2.1: Atomic Simulation Techniques

Atomistic simulations have become essential tools in modern materials research, enabling the prediction and analysis of physical properties at the scale of individual atoms. These methods provide insight into material behavior by solving Newtonian or quantum-mechanical equations of motion for large ensembles of atoms. Among the most widely used techniques are Molecular Dynamics and Molecular Statics, each with distinct capabilities and applications.

2.1.1 Molecular Dynamics vs Molecular Statics

Molecular Dynamics (MD) simulates the physical motion of atoms over time by numerically integrating Newton's second law of motion [20]. Interatomic forces are calculated at each time step using a selected potential energy model, allowing the system to evolve dynamically [20]. MD simulations are particularly useful for investigating time-dependent

phenomena such as thermal vibrations, phase transformations, defect migration, and dislocation motion [21]. By incorporating thermostats and barostats, MD can simulate systems under various temperature and pressure conditions, making it a powerful tool for studying finite-temperature behavior [22]. However, MD simulations are computationally expensive due to the need to resolve atomic motions on the order of femtoseconds. Consequently, accessible simulation timescales are typically limited to nanoseconds, which may not be sufficient to observe slow processes or large-scale structural changes in complex alloys [21].

Molecular Statics (MS), in contrast, focuses on the equilibrium properties of a system by minimizing its total potential energy [23]. MS is well-suited for evaluating structural properties such as lattice parameters, elastic constants, and generalized stacking fault energies under static conditions (typically at 0 K) [24]. Because it avoids time integration, MS is generally more computationally efficient than MD, enabling the use of larger atomic models and more complex chemistries [23].

2.2 Density Functional Theory (DFT)

DFT is a first-principles quantum mechanical modeling method widely regarded as the gold standard for atomistic property prediction [25]. Rather than solving the many-body Schrödinger equation directly, DFT reformulates the problem in terms of the electron density as the central variable, based on the foundational work by Hohenberg, Kohn, and Sham [26] and is generalized by the Kohn-Sham Equation [27]:

$$\varepsilon_i \psi_i(r) = \left[-\frac{\hbar^2}{2m} \nabla^2 + V_{\text{ext}}(r) + V_{\text{H}}(r) + V_{\text{XC}}(r) \right] \psi_i(r)$$

Where $\psi_i(r)$ is the Kohn-Sham orbitals (single-particle wavefunction), ε_i is the eigenvalue (energy) of the i$^{\text{th}}$ orbital, $V_{ext}(r)$ is the external potential (e.g., from nuclei), $V_H(r)$ is the Hartree potential (classical electron-electron repulsion), $V_{XC}(r)$ is the exchange-correlation potential (quantum corrections), and $\frac{\hbar^2}{2m}\nabla^2$ is the kinetic energy operator of a non-interacting electron.

DFT allows for the calculation of total energy, atomic forces, stress tensors, and electronic properties with high accuracy across a wide range of materials [28]. In the context of multi-component alloys, DFT enables detailed analysis of bonding behavior, charge distribution, and phase stability at the atomic scale [29]. However, the method is computationally intensive, especially as the system size increases [30].

For systems containing more than a few hundred atoms, DFT becomes impractical due to its unfavorable scaling with respect to atom count [30]. This limitation restricts its application in large-scale simulations, such as those required to evaluate temperature-dependent properties or model realistic microstructures. Furthermore, the need to run multiple configurations (e.g., slip systems for GSFE or supercells for elastic constant prediction) further compounds computational demands.

Despite these constraints, DFT remains a critical reference method. In this study, it is used to benchmark the accuracy of machine-learned potentials across key properties, including lattice parameters, elastic constants, and generalized stacking fault energies for CoNiRu-based alloys.

2.3 Interatomic Potential Models

Interatomic potentials define how atoms interact within a material by assigning energy to different atomic configurations. The accuracy of any atomistic simulation hinges on the fidelity of the chosen potential model [31]. Interatomic potentials offer computational efficiency but limited accuracy, while modern techniques like DFT and MLIPs offer higher precision—at greater computational cost or complexity [32]. This section outlines the theoretical background for both DFT and MLIPs, culminating in the uMLIP used in this study.

2.3.1 Traditional Interatomic Potentials

Traditional interatomic potential serves as the foundation of classical atomistic simulations and has been extensively used to model a wide range of materials [33]. These models rely on analytically derived mathematical expressions to approximate the total energy of a system based on atomic positions. While their accuracy is limited compared to first-principles methods like DFT, traditional potentials offer significant computational advantages, making them suitable for large-scale simulations [34]. Some of the most widely adopted traditional potentials include:

- **Lennard-Jones (LJ) Potential:** The Lennard-Jones potential is one of the simplest and most well-known models used to describe non-bonded interactions between atoms or molecules. It is defined as a pairwise potential of the form [35]:

$$V(r) = 4\varepsilon\left[\left(\frac{\sigma}{r}\right)^{12} - \left(\frac{\sigma}{r}\right)^{6}\right]$$

where r is the distance between two atoms, ε represents the depth of the potential well (indicating interaction strength), and σ is the finite distance at which the interparticle potential is zero. The first term models short-range Pauli repulsion, while the second term models long-range van der Waals attraction. Although originally developed to describe noble gases like argon, the LJ potential is frequently used as a pedagogical model and for studying fundamental physical phenomena such as phase transitions, diffusion, and defect dynamics [36]. However, its simplicity also limits its realism: it cannot account for directional bonding, charge transfer, or many-body effects, making it unsuitable for metallic or covalently bonded materials [37].

- **Embedded Atom Method (EAM):** EAM is one of the most widely used interatomic potential models for simulating metallic systems. Originally developed by Daw and Baskes, EAM incorporates the concept of embedding an atom into the electron density field created by its neighbors [38]. The total energy, E, of the system is expressed as:

$$E = \sum_{i} F_i\left(\rho_i\right) + \frac{1}{2}\sum_{i \neq j} \phi_{ij}\left(r_{ij}\right)$$

where $F_i(\rho_i)$ is the embedding energy of atom i as a function of the local electron density p_i, and $\phi_{ij}(r_{ij})$ represents the pairwise interaction between atoms i and j at a distance r_{ij}. In contrast to simple pair potentials, EAM captures the collective effects of neighboring atoms, allowing for more accurate predictions of mechanical behavior, defect formation energies, and cohesive properties in metallic alloys [39]. EAM has been successfully applied to a wide range of FCC and HCP metals and their binary or ternary compounds [40]. However, its applicability to complex multi-component systems is contingent upon the availability of reliable cross-element parameterizations.

For the CoNiRu system, a parameter set that includes all relevant element pairs is required to ensure thermodynamic and mechanical consistency across the alloy configurations.

- **Modified Embedded Atom Method (MEAM):** MEAM extends the original EAM framework by incorporating angular-dependent interactions, thereby improving its applicability to materials with non-close-packed structures or directional bonding [41]. MEAM retains the general structure of EAM but introduces an angular screening function that accounts for the directional dependence of bonding, making it particularly useful for modeling HCP phases, stacking faults, and anisotropic defect behavior [42]. The total energy in MEAM is similarly composed of embedding and pairwise interaction terms but includes additional terms to capture angular dependence and second-nearest neighbor effects. The total energy, E, of a system in MEAM is expressed as:

$$E = \sum_i F_i\left(\bar{p}_i\right) + \frac{1}{2}\sum_{i \neq j} S_{ij}\phi_{ij}\left(R_{i_j}\right)$$

Where $F_i(\bar{p}_i)$ the embedding energy of atom i as a function of the local electron density $\bar{\rho}_i$, $\phi_{ij}(R_{ij})$ is the pair potential between atoms i and j, S_{ij} is the screening functioning account for angular dependence and blocking by other atoms, and R_{ij} is the distance between atoms i and j. This expanded formalism enables MEAM to better represent low-symmetry environments and directional bonding variations that are prevalent in complex alloys and intermetallic structures [42]. Unlike EAM, MEAM uses a modified electron density that includes angular contributions:

$$\bar{p}_i = \rho_i^{(0)} \cdot G(\Gamma_i)$$

Where $\rho_i^{(0)}$ is the spherically averaged electron density (similarly to ρ_i in EAM) and $G(\Gamma_i)$ is the angular correction function dependent on the angular contribution Γ_i in which:

$$\Gamma_i = \sum_{k=1}^{3} t^{(k)}\left(\frac{p_i^{(k)}}{\rho_i^{(0)}}\right)^2$$

Where $\rho_i^{(k)}$ is the higher-order angular partial electron density and $t^{(k)}$ is the adjustable weighting parameters for each angular component. To model directional bonding, MEAM includes the screening function:

$$S_{ij} = \prod_{k=i_j} S_{ik_j}$$

Where S_{ij} accounts for whether atom k screens the interaction between atoms i and j. If another atom lies between i and j it can partially or fully screen the interaction. In the context of the CoNiRu system, MEAM offers potential advantages over EAM in accurately modeling the HCP phase and capturing the energetic landscape of stacking faults and slip planes [43][44]. However, the added complexity comes with increased sensitivity to parameter quality and computational cost [43][44].

- **Tersoff and Stillinger-Weber (SW) Potentials:** These potentials include many-body and angular terms and are commonly used for covalently bonded materials such as silicon and carbon-based systems [45][46].

Although these models provide fast and relatively accurate simulations within their fitted domains, they suffer from limited transferability [47]. Parameters are typically tuned to experimental or DFT data for specific materials, which constrains their ability to generalize to different compositions, crystal structures, or thermodynamic conditions. Despite these limitations, traditional potentials remain essential tools in multiscale modeling workflows. They are often used for initial screening, microstructure evolution studies, or as a baseline for evaluating more advanced models, such as MLIPs [48].

2.3.2 Machine Learning Interatomic Potentials (MLIPs)

MLIPs provide a powerful solution to the trade-off between accuracy and scalability. These models are trained on large datasets—often composed of DFT-calculated energies, forces, and stresses—using regression techniques such as Gaussian process regression, decision trees, or neural networks [31]. Once trained and validated, MLIPs can generalize to new atomic configurations with high fidelity and execute simulations on length and time scales inaccessible to DFT [49].

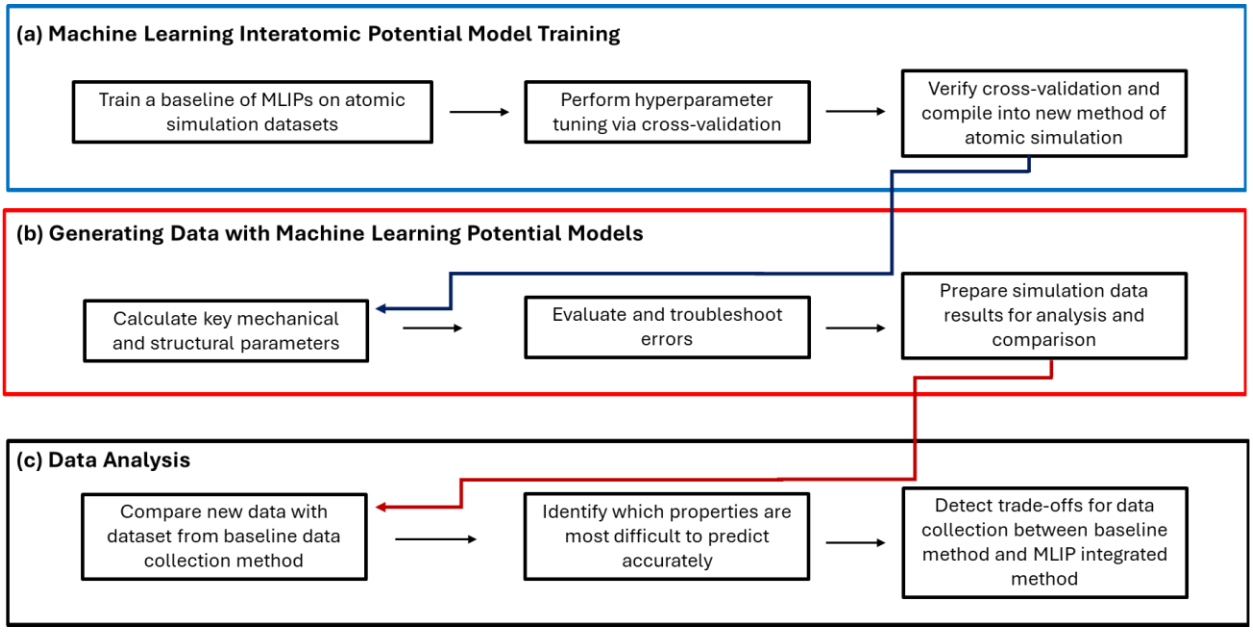

Figure 2: MLIP Training Flow Chart

Unlike traditional potentials, MLIPs do not rely on predefined analytical forms. Instead, they learn complex relationships directly from quantum mechanical data, capturing subtle features such as angular dependence, coordination variability, and charge transfer effects. This flexibility allows MLIPs to adapt to a wider range of chemistries and structures, making them particularly suitable for modeling multi-principal element alloys like CoNiRu [50].

In practice, the training process involves selecting a representative dataset, defining a descriptor for atomic environments (e.g., symmetry functions or graph-based representations), and optimizing the model to reproduce target quantities. The resulting MLIP can then be integrated into atomistic simulation engines like LAMMPS for energy minimization, molecular dynamics, or property evaluation.

2.3.3 Universal Machine Learning Interatomic Potentials (uMLIPs)

uMLIP extends the capabilities of conventional MLIPs by being trained on datasets that span a broad range of elements, compositions, and structures [51]. Unlike system-specific MLIPs, which are tuned for one alloy or crystal type, uMLIPs trade some accuracy for greater generality and transferability. This makes them highly attractive for applications in alloy discovery and materials screening, where exhaustive retraining for each new system is impractical [52].

In this work, the uMLIP employed is based on the SevenNet framework— a scalable, equivariant graph neural network trained on both published and unpublished DFT data for over 60 elements, including Co, Ni, Ru, and their binaries and ternaries [53]. SevenNet is designed to encode the physics of atomic interactions while preserving symmetries in the data, such as translational and rotational invariance.

The uMLIP model was compiled for use with LAMMPS and evaluated for its ability to reproduce three key atomistic properties—lattice constants, elastic constants, and GSFE curves—across multiple CoNiRu compositions, structural phases (FCC and HCP), and temperatures (0 K and 300 K). The reliability of this approach is determined by comparing uMLIP-predicted results to available DFT data, thus assessing the model's effectiveness in simulating chemically complex systems with practical accuracy and efficiency.

2.3 Computational Framework and DFT Benchmarking

To evaluate the performance of the uMLIP, this study integrates advanced simulation tools and standardized benchmarking practices. The simulation environment combines the scalable uMLIP model, implemented via the SevenNet architecture, with the LAMMPS. This section outlines the computational setup and the strategy for validating uMLIP predictions against DFT data.

2.3.1 Simulation Environment: SevenNet and LAMMPS

The uMLIP used in this work is implemented through SevenNet, a scalable and equivariant graph neural network-based interatomic potential framework. SevenNet is trained on a diverse chemical space, encompassing over 60 elements and thousands of atomic configurations [53]. The training data include both published and unpublished DFT calculations, specifically curated to capture a wide range of physical environments, bonding types, and crystal structures. Co, Ni, Ru, and their binary and ternary combinations are explicitly represented in the training dataset, enhancing the model's applicability to the CoNiRu alloy system.

SevenNet outputs were compiled into a model compatible with LAMMPS, an open-source molecular simulation package maintained by Sandia National Laboratories. LAMMPS is optimized for parallel computation and supports large-scale molecular statics and dynamics simulations, making it suitable for evaluating systems consisting of tens of thousands of atoms

[54]. Simulations were executed on the OU Supercomputing Center for Education and Research (OSCER), allowing efficient evaluation of multi-thousand-atom supercells under different structural and thermal conditions. The integrated SevenNet–LAMMPS framework enables the calculation of lattice parameters amd elastic constants at both 0 K and 300 K and GSFE at 0 K for multiple CoNiRu-based systems.

2.3.2 Overview of DFT Data and Validation Strategy

To benchmark the performance of the uMLIP model, simulation results are compared to reference data obtained from DFT calculations. The DFT dataset used for validation consists of both peer-reviewed publications and unpublished results generated by collaborators for this project. The benchmarking is conducted across the following categories:

- **Lattice Parameters**: DFT-derived equilibrium lattice constants for FCC and HCP CoNiRu alloys, as well as for Co_2Ni_2Ru, $CoNiRu_2$, and pure Ni.
- **Elastic Constants**: Stress-strain derived stiffness matrices from static DFT calculations. In the case of hexagonal structures, effective elastic constants are computed and converted from the $[1\bar{1}0] - [11\bar{2}] - [111]$ system to the standard $[100] - [010] - [001]$ orientation for direct comparison.
- **GSFE Profiles**: Generalized stacking fault energy curves are extracted by simulating atomic displacements across common slip planes and directions. These DFT curves serve as ground truth for evaluating uMLIP-predicted GSFE behavior.

Where available, **experimental data** from X-ray diffraction or mechanical testing are also used as an additional reference—particularly for validating 300 K lattice parameters. The comparison framework is structured to assess both **absolute accuracy** (e.g., % deviation from DFT values) and **predictive trends** (e.g., structural or temperature-dependent behavior) to determine the viability of uMLIP as a replacement or supplement to DFT in large-scale material simulations.

Chapter 3: Alloy Systems and Simulation Set-Up

3.1 Materials and Compositions

This study focuses on the atomistic evaluation of a series of ternary and unitary metallic systems composed of cobalt (Co), nickel (Ni), and ruthenium (Ru). These elements were selected based on their combined known stability in high-performance alloy systems, particularly those designed for elevated temperature applications in aerospace, nuclear, and structural environments [17]. The central objective is to investigate how different elemental ratios, crystal structures, and temperatures affect the mechanical and defect-related properties of these systems.

The following compositions were selected for systematic simulation:

- **CoNiRu** – an equiatomic ternary alloy (1:1:1 ratio) representative of chemically balanced solid solutions.
- **Co_2Ni_2Ru** – a Co- and Ni-rich variant (2:2:1 ratio), intended to explore excess transition metal effects on structural stability and elasticity.
- **$CoNiRu_2$** – a Ru-rich variant (1:1:2 ratio), providing insight into the influence of heavier and more refractory elements.
- **Pure Ni** – a unitary system used as a baseline for comparison, due to its well-documented properties and common usage in benchmark studies.

Each of these compositions are modeled in both FCC and HCP crystal structures. This dual-phase evaluation enables a detailed understanding of phase-dependent behavior and allows for the assessment of potential structural transitions or metastability under varying thermodynamic conditions. Table 3.1 summarizes the elemental compositions and structural phases considered in this study:

Table 1: Simulated Materials and Crystal Structures

Material	Composition (%)	Crystal Structure	Notes
CoNiRu	Co: 33.3, Ni: 33.3, Ru: 33.3	FCC, HCP	Equi-atomic ternary system

Co_2Ni_2Ru	Co: 40.0, Ni: 40.0, Ru: 20.0	FCC	Co- and Ni-rich alloy
$CoNiRu_2$	Co: 25.0, Ni: 25.0, Ru: 50.0	HCP	Ru-rich alloy
Pure Ni	Ni: 100.0	FCC	Benchmark/Control metal

In the CoNiRu alloy system, both FCC and HCP crystal structures can be stabilized depending on the relative atomic ratios of Co, Ni, and Ru. This polymorphic behavior arises from the competing structural tendencies of the constituent elements. Nickel (Ni) naturally crystallizes in the FCC structure, while cobalt (Co) exhibits allotropic behavior, favoring HCP at lower temperatures and FCC at elevated temperatures. Ruthenium (Ru), by contrast, strongly favors the HCP structure due to its electronic configuration and bonding characteristics [55] [56]. In equiatomic CoNiRu compositions, the FCC phase is typically stabilized due to the dominant FCC-forming tendency of Ni and the elevated temperature behavior of Co, in conjunction with the high configurational entropy of the ternary system. However, as the Ru content increases, the structural preference shifts. As demonstrated in $CoNiRu_2$, the higher atomic fraction of Ru (approximately 66.7%) promotes stabilization of the HCP phase. This shift is attributed to both the intrinsic HCP-stabilizing nature of Ru and the increased lattice distortion and elastic strain energy incurred when attempting to accommodate the larger Ru atoms in an FCC lattice. Furthermore, the anisotropic bonding behavior of Ru, along with its electronic band structure, further favors the HCP phase, making it energetically more favorable than FCC in Ru-rich compositions.

3.2 Crystal Structures and Temperatures Studied

The atomic-scale properties of metallic systems are highly sensitive to crystal structure and temperature [57]. In this study, each alloy composition is modeled in both FCC and HCP phases where applicable, to capture the influence of lattice symmetry and atomic packing on mechanical behavior.

- FCC structures are prevalent in ductile metals such as Ni and Co at ambient temperatures, and they typically exhibit high stacking fault energies and isotropic elastic behavior.
- HCP structures, while less symmetric, are characteristic of certain Co-rich and Ru-rich phases. HCP metals often show directional dependence in mechanical properties and can exhibit lower symmetry defect structures.

Both FCC and HCP structures were constructed using ideal lattice configurations and subjected to full relaxation during simulation. Simulations were conducted at two distinct temperatures:

- 0 K (absolute zero), representing ground-state configurations for direct comparison with static DFT calculations.
- 300 K, representing ambient temperature and providing insight into finite-temperature effects using molecular dynamics techniques.

This dual-phase, dual-temperature design enables comprehensive evaluation of temperature-dependent behavior and structure-sensitive trends in lattice constants, elastic moduli, and fault energetics.

Chapter 4: Property Calculation Methodology

4.1 Lattice Parameter Calculation

The lattice parameters of CoNiRu-based alloys were calculated using atomistic simulations in LAMMPS with a uMLIP called SevenNet. At 0 K, the process began by selecting a reasonable initial lattice parameter based on values reported in prior literature. Using this input, crystal structures were constructed in both FCC and HCP configurations. The simulation box was then filled with atoms arranged according to the trial lattice parameter. Energy minimization was applied to relax the atoms to their lowest energy configuration. This process was repeated across several slightly varied lattice constants. By comparing the total energies resulting from each configuration, the lattice parameter corresponding to the lowest total energy was identified as the equilibrium value at 0 K. This approach ensures the simulation captures the most energetically favorable atomic arrangement without thermal interference [14][58][59][60].

For lattice parameter calculations at 300 K, the relaxed 0 K structures were used as starting points. These structures were then simulated under constant pressure and temperature conditions. After reaching thermal equilibrium, the average lattice dimension was measured from the simulation output. The extracted lattice parameters reflect thermal expansion effects and allow comparison to experimental or DFT results conducted at ambient temperature.

4.2 Elastic Constant Calculation

Elastic constants were extracted from simulations by applying small deformations to relaxed crystal structures and analyzing the resulting stress response. Elastic constants were computed using a small-strain approach. Incremental strain tensors were applied to the relaxed supercell, and the resulting stress tensors were calculated using the virial theorem. The elastic stiffness tensor C_{ij} was derived by fitting the linear stress-strain relationship:

$$\sigma_i = C_{ij} \cdot \varepsilon_j$$

Where σ_i and ε_j represent stress and strain components, respectively. For cubic systems (FCC), the independent elastic constants C_{11} , C_{12} and C_{44} were extracted. For hexagonal systems (HCP), additional constants such as C_{13}, C_{33}, and C_{66} were also evaluated. These constants serve as critical indicators of stiffness, mechanical stability, and anisotropy. They also provide essential validation targets in comparison with DFT benchmarks.

At 0 K, simulations were conducted on structures previously minimized to equilibrium using the selected lattice parameter. Strains were applied to the simulation cell, and after each deformation, the atomic system was relaxed through energy minimization [14][58][59][60]. Stress tensors were then computed for each strained configuration. These stress–strain data sets were used to calculate the second-order elastic constants. In cases where the local crystal orientation deviated from the standard cubic axis, results were converted from the $[1\bar{1}0] - [11\bar{2}] - [111]$ coordinate system to the conventional $[100] - [010] - [001]$ system for consistency. The Elastic Constant ($C_{11,}\, C_{12,}\, C_{44}$) data for all FCC system calculated is then converted into Effective Elastic Constant ($C_{11,}^{\dagger}\, C_{12}^{\dagger,}\, C_{44}^{\dagger}$) via:

$$C_{11}^{\dagger} = \frac{C_{11} + C_{22} + C_{33}}{3}$$

$$C_{12}^{\dagger} = \frac{C_{12} + C_{13} + C_{23}}{3}$$

$$C_{44}^{\dagger} = \frac{C_{44} + C_{55} + C_{66}}{3}$$

This was done to better organize the elastic constant data and for ease of comparison with the DFT elastic constant data.

To determine elastic constants at 300 K, the same methodology was applied, but instead of zero-temperature relaxation, simulations were run dynamically at finite temperature using the NVT ensemble [14][58][59][60]. The structures were first equilibrated at 300 K, then strained incrementally. Time-averaged stress values were computed for each strain state, enabling elastic constants to be calculated under thermally active conditions. The 300 K calculations account for atomic vibrations and thermal fluctuations and provide a more realistic assessment of mechanical response at ambient temperature.

4.3 Generalized Stacking Fault Energy Calculation

The GSFE quantifies the energy landscape encountered by atomic planes as they shear past one another, playing a central role in dislocation nucleation and motion. The GSFE surface is particularly important in assessing slip behavior and partial dislocation formation in FCC and HCP crystals.

To compute the GSFE, a crystallographic slip plane was selected, typically the [111] plane for FCC structures and the [0001] plane for HCP structures. The simulation cell was cleaved along this plane, and one half of the structure was rigidly displaced relative to the other in incremental steps along the slip direction—this was done for a total of 10 planes per alloy. After each displacement, atomic positions were relaxed perpendicular to the fault plane, while

the in-plane displacement was constrained. The stacking fault energy γ at each displacement u is calculated as:

$$\gamma(\mathrm{u}) = \frac{E(u) - E_0}{A}$$

where $E(u)$ is the total energy of the sheared configuration, E_0 is the energy of the relaxed perfect crystal, and A is the area of the fault plane. The resulting GSFE curve provides information on:

- Intrinsic stacking fault energy (ISF): local minima.
- Unstable stacking fault energy (USF): energy barriers to slip.
- Slip path periodicity: degree of lattice recovery after full dislocation movement.

These features are used directly in the assessment of local slip resistance and mechanical anisotropy.

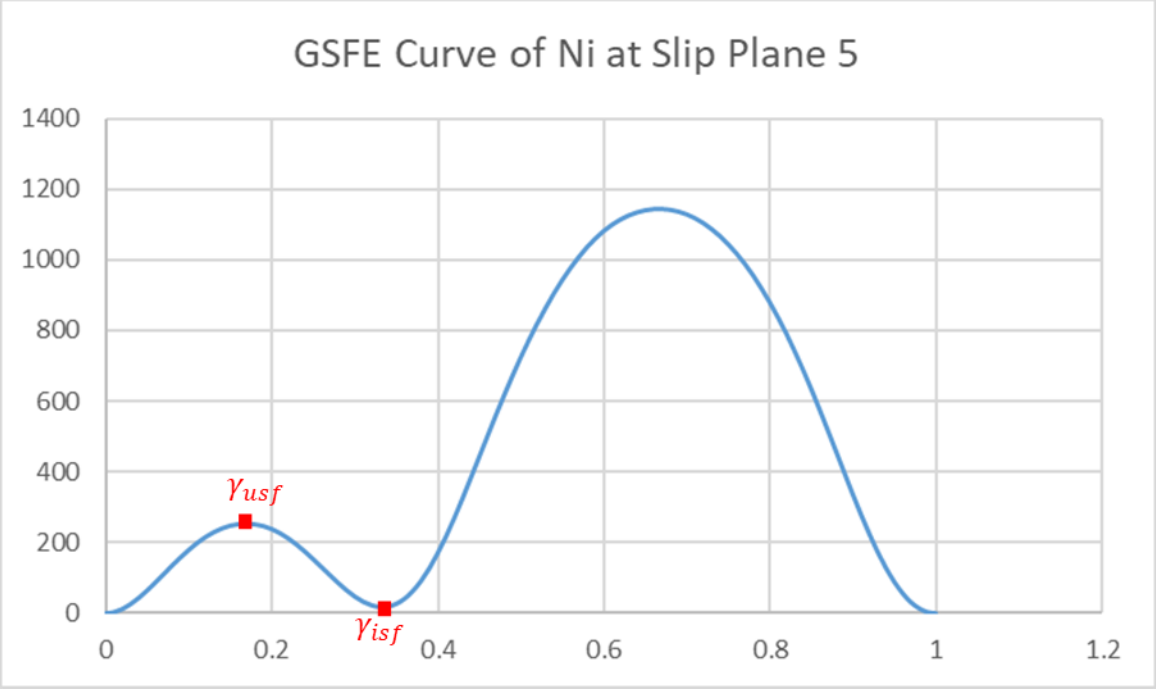

Figure 3: USF and ISF From GSFE Curve Example

GSFE curves were calculated at 0 K for FCC and HCP CoNiRu structures. The procedure involved constructing a simulation cell containing a predefined slip plane relevant to each crystal

structure [14][58]. The system was first relaxed using energy minimization to ensure stability. The crystal was then divided along the slip plane, and the upper half was displaced incrementally over the lower half along a specified crystallographic direction associated with slip. After each displacement step, the system was re-minimized while keeping the top and bottom atomic layers fixed to prevent rigid-body motion [59][60]. The potential energy was recorded for each displacement. This process was repeated until the full periodic slip distance was covered. The GSFE curve was constructed by plotting the energy per unit area versus the applied displacement. The unstable stacking fault energy γ_{usf} and intrinsic stacking fault energy γ_{isf} can be determined from the GSFE curve by identifying the first local maximum and the following local minimum, respectively, as demonstrated in Figure 3 . This curve characterizes the energy barrier for dislocation motion across the slip plane [61]. The GSFE values obtained from the uMLIP-based simulations were then compared to reference DFT values.

Chapter 5: Results & Analysis

5.1 Lattice Parameter Comparisons

This section presents the calculated lattice parameters for each alloy system evaluated using the uMLIP model, compared directly against reference values obtained from DFT calculations and experimental measurements where available. Simulations were performed using molecular statics with large-scale atomic models at both 0 K and 300 K, across FCC and HCP phases as applicable.

5.1.1 CoNiRu: uMLIP vs DFT

For the equiatomic CoNiRu alloy, the lattice parameters were calculated using both DFT and uMLIP approaches in FCC and HCP phases at 0 K. The equilibrium lattice parameter of an FCC CoNiRu six-atom structure was reported to be 3.61 Å [62].

Table 2: CoNiRu uMLIP Lattice Parameter Data

Material	Structure	Temp (K)	Lattice Parameter a (Å)	Lattice Parameter c (Å)	c/a Ratio
CoNiRu	FCC	0	3.638	N/A	N/A

		300	3.721	N/A	N/A
CoNiRu	HCP	0	2.570	4.168	1.622
		300	2.600	4.115	1.582

The uMLIP simulation for FCC CoNiRu at 0K was conducted using a 6,750-atom simulation. The predicted lattice parameter from this simulation was found to be within ±0.7% of the corresponding DFT value, indicating strong agreement with first-principles results. In contrast, the HCP CoNiRu system at 0K was modeled using a significantly larger 20,800-atom supercell. However, due to the absence of a DFT benchmark for the HCP phase, only the uMLIP-predicted lattice parameter is reported for this configuration. These results demonstrate that the uMLIP model accurately reproduces the equilibrium lattice parameter for FCC CoNiRu at 0 K within an acceptable margin of error. The near agreement validates the uMLIP's capability to capture volumetric behavior for this specific composition and structure.

5.1.2 Co_2Ni_2Ru: uMLIP vs. DFT/Experiment

Table 3:Co_2Ni_2Ru uMLIP Lattice Parameter Data

Material	**Structure**	**Temp (K)**	**Lattice Parameter a (Å)**
Co_2Ni_2Ru	FCC	0K	3.663
		300K	3.702

For the FCC Co_2Ni_2Ru system, lattice parameters were evaluated at both 0 K and 300 K to assess the accuracy and transferability of the uMLIP model. At 0 K, a DFT benchmark using a 120-atom configuration (unpublished) result of 3.58 Å [58] served as the reference for validating the uMLIP results. The uMLIP simulation, performed with a significantly larger 11,664-atom supercell, produced a lattice parameter within ±2.3% of the DFT value, indicating good agreement. At 300 K, experimental data obtained via X-ray diffraction reported a lattice parameter of 3.59 Å [63]. The uMLIP simulation at this temperature, also conducted with the same 11,664-atom supercell, predicted a lattice parameter within ±3.0% of the experimental measurement. These results affirm the robustness of the uMLIP model in capturing lattice

behavior across temperatures and demonstrate its applicability to non-equiatomic Co-Ni-Ru compositions.

5.1.3 $CoNiRu_2$: uMLIP Only

Table 4: $CoNiRu_2$ uMLIP Lattice Parameter Data

Material	Structure	Temp (K)	Lattice Parameter a (Å)	Lattice Parameter c (Å)	c/a Ratio
$CoNiRu_2$	HCP	0K	2.608	4.226	1.62
		300K	2.616	4.241	1.621

The $CoNiRu_2$ HCP system was simulated at both 0 K and 300 K using 20,800-atom supercells to evaluate its structural behavior. Due to the lack of available DFT data for this composition and phase, the results from the uMLIP simulations are reported as standalone predictions. While no direct benchmarking is possible, these simulations provide useful insight into the structural characteristics of $CoNiRu_2$ in the HCP phase across different temperatures.

5.1.4 Pure Ni

Table 5: Pure Ni uMLIP Lattice Parameter Data

Material	Structure	Temp (K)	Lattice Parameter a (Å)
Pure Ni	FCC	0K	3.503
		300K	3.516

For pure Ni in the FCC structure at 0 K, the DFT reference value is 3.519 Å [64]. The uMLIP simulation, conducted using a 6,750-atom supercell, predicted a lattice parameter within ±0.5% of the DFT result. This high level of agreement confirms the strong accuracy of the uMLIP model in single-element systems and establishes it as a reliable baseline for comparative analysis across more complex alloy systems.

5.2 Elastic Constant Comparisons

Elastic constants are essential for understanding mechanical stability, stiffness, and anisotropy in crystalline solids. This section compares the elastic constant predictions from the uMLIP model to available DFT results. The evaluation includes multiple compositions and

structural phases across 0 K and 300 K, providing insight into the model's transferability and accuracy under varying atomic environments.

5.2.1 CoNiRu: uMLIP vs. DFT

Table 6: FCC CoNiRu DFT Elastic Constant Data @ 0K

DFT FCC CoNiRu @ 0K	
Effective Elastic Constants	**Average Values (GPa)**
$\mathbf{C_{11}^{\dagger}}$	404.43
$\mathbf{C_{12}^{\dagger}}$	165.85
$\mathbf{C_{44}^{\dagger}}$	147.03

The DFT reference data from another FCC CoNiRu structure, based on 120-atom cells, involved averaging elastic constants over 13 distinct configurations [65].

Table 7: FCC CoNiRu uMLIP Elastic Constant Data @ 0K

uMLIP FCC CoNiRu @ 0K	
Effective Elastic Constants	**Average Values (GPa)**
$\mathbf{C_{11}^{\dagger}}$	190.5
$\mathbf{C_{12}^{\dagger}}$	248.23
$\mathbf{C_{44}^{\dagger}}$	79.77

For FCC CoNiRu at 0 K, simulated with a 6,750-atom supercell, the uMLIP predictions deviated significantly from known DFT values. No consistent pattern of overestimation or underestimation was observed across elastic constants C_{11}, C_{12}, or C_{44}, highlighting limitations in the force-field training, particularly regarding mechanical properties in complex ternary systems.

$$C = \begin{bmatrix} 256.81 & 202.89 & 203.16 & 0.22 & 0.11 & 0.01 \\ 202.89 & 256.56 & 202.79 & -0.34 & 0.11 & -0.11 \\ 203.16 & 202.79 & 257.76 & 0.02 & 0.45 & -0.08 \\ 0.22 & -0.34 & 0.02 & 83.13 & 0.13 & 0.07 \\ 0.11 & 0.11 & 0.45 & 0.13 & 83.35 & -0.07 \\ 0.01 & -0.11 & -0.08 & 0.07 & -0.07 & 83.16 \end{bmatrix} [GPa]$$

Figure 4: FCC CoNiRu uMLIP Elastic Constant Data @ 300K

$$C = \begin{bmatrix} 170.55 & 263.70 & 50.23 & 102.17 & -83.74 & -23.39 \\ 263.70 & 554.86 & 438.89 & 66.44 & -45.78 & -27.05 \\ 50.23 & 438.89 & 532.70 & -58.99 & -9.65 & -68.71 \\ 102.17 & 66.44 & -58.99 & 97.11 & -12.18 & 80.77 \\ -83.74 & -45.78 & -9.65 & -12.18 & 73.78 & -65.62 \\ -23.39 & -27.05 & -68.71 & 80.77 & -65.62 & 46.09 \end{bmatrix} [GPa]$$

Figure 5: HCP CoNiRu uMLIP Elastic Constant Data @ 0K

$$C = \begin{bmatrix} 276.05 & 194.30 & 163.31 & 0.28 & -0.54 & 0.70 \\ 194.30 & 274.22 & 162.22 & 0.22 & 0.53 & -0.28 \\ 163.31 & 162.22 & 344.42 & 0.16 & 0.06 & 1.02 \\ 0.28 & 0.22 & 0.16 & 57.51 & -0.08 & -0.61 \\ -0.54 & 0.53 & 0.06 & -0.08 & 57.62 & -0.06 \\ 0.70 & -0.28 & 1.02 & -0.61 & -0.06 & 41.22 \end{bmatrix} [GPa]$$

Figure 6: HCP CoNiRu uMLIP Elastic Constant Data @ 300K

Elastic constant data were collected for several CoNiRu configurations using the uMLIP model; however, DFT reference values were either unavailable or insufficient for direct benchmarking. Figures 4, 5, and 6 present raw elastic constant data simulated using uMLIP for FCC CoNiRu at 300 K and HCP CoNiRu at both 0 K and 300 K—all simulated using 11664 atoms. These elastic constant results were not further converted into effective elastic constants due to the lack of available DFT benchmark data. As a result, they are included for completeness but should be considered exploratory and used only for internal comparisons or future validation.

5.2.2 Co_2Ni_2Ru: uMLIP vs. DFT

Table 8: FCC Co_2Ni_2Ru DFT Elastic Constant Data @ 0K

DFT FCC Co_2Ni_2Ru @ 0K	
Effective Elastic Constants	**Average Values (GPa)**
$\mathbf{C_{11}^{\dagger}}$	401.078
$\mathbf{C_{12}^{\dagger}}$	168.944
$\mathbf{C_{44}^{\dagger}}$	148.554

An unpublished DFT reference for the FCC structure using 120-atom cells serves as the benchmark for evaluating simulation results at 0 K [58]. This data table provides a critical point of comparison for assessing the accuracy of uMLIP predictions underground-state conditions.

Table 9: FCC Co_2Ni_2Ru uMLIP Elastic Constant Data @ 0K

uMLIP FCC Co_2Ni_2Ru @ 0K	
Effective Elastic Constants	**Average Values (GPa)**
$\mathbf{C_{11}^{\dagger}}$	228.307
$\mathbf{C_{12}^{\dagger}}$	114.800
$\mathbf{C_{44}^{\dagger}}$	108.510

For FCC Co_2Ni_2Ru at 0 K, the uMLIP simulation using an 11,664-atom supercell exhibited large deviations from the DFT benchmark. Similar to the behavior observed in CoNiRu, the uMLIP model did not display a consistent trend of over- or underestimation across elastic constants. This lack of systematic bias suggests poor reproducibility of stiffness trends, indicating limitations in the model's ability to accurately capture mechanical properties in complex alloy systems.

$$C = \begin{bmatrix} 260.35 & 195.26 & 194.99 & 0.16 & 0.10 & 0.07 \\ 195.26 & 260.67 & 195.21 & -0.21 & 0.00 & 0.65 \\ 194.99 & 195.21 & 260.82 & -0.05 & -0.17 & 0.33 \\ 0.16 & -0.21 & -0.05 & 92.97 & -0.04 & -0.02 \\ 0.10 & 0.00 & -0.17 & -0.04 & 92.87 & 0.15 \\ 0.07 & 0.65 & 0.33 & -0.02 & 0.15 & 92.66 \end{bmatrix} [GPa]$$

Figure 7: FCC Co_2Ni_2Ru uMLIP Elastic Constant Data @ 300K

Elastic constant data were also collected for FCC Co_2Ni_2Ru at 300 K using the uMLIP model, as shown in Figure 7. The simulation was performed using an 11,664-atom supercell. However, due to the absence of corresponding DFT benchmark data for this composition and temperature, the raw elastic constant results were not further converted into effective elastic constants. While the results exhibit internal consistency within the model, they must be interpreted with caution due to the lack of external validation.

5.2.3 $CoNiRu_2$: uMLIP Only

Table 10: HCP $CoNiRu_2$ uMLIP Elastic Constant Data @ 0K

DFT $CoNiRu_2$ @ 0K	
Effective Elastic Constants	**Average Values (GPa)**
$\mathbf{C_{11}^{\dagger}}$	279.280
$\mathbf{C_{12}^{\dagger}}$	123.837
$\mathbf{C_{44}^{\dagger}}$	46.293

Table 11: HCP $CoNiRu_2$ uMLIP Elastic Constant Data @300K

MLIP $CoNiRu_2$ @ 300K	
Effective Elastic Constants	**Average Values (GPa)**
$\mathbf{C_{11}^{\dagger}}$	301.110
$\mathbf{C_{12}^{\dagger}}$	189.107
$\mathbf{C_{44}^{\dagger}}$	39.74

For HCP $CoNiRu_2$ at both 0 K and 300 K, uMLIP simulations were conducted using 20,800-atom supercells. In the absence of published DFT or experimental elastic constant data for this composition, the calculated values are presented as preliminary predictions. Without external validation, these results cannot be quantitatively benchmarked and should be considered exploratory in nature.

5.2.4 Pure Ni: uMLIP vs. DFT

Table 12: Pure Ni DFT Elastic Constant Data @ 0K

DFT Ni @ 0K	
Elastic Constants	**Average Values (GPa)**
$\mathbf{C_{11}}$	401.078
$\mathbf{C_{12}}$	168.944
$\mathbf{C_{44}}$	148.554

The DFT reference [64], based on a 4-atom FCC Ni cell at 0 K, provides well-established elastic constants that serve as a reliable benchmark. These values are used to validate the accuracy of uMLIP predictions for pure Ni.

Table 13: Pure Ni uMLIP Elastic Constant Data @ 0K

uMLIP Ni @ 0K		
Effective Elastic Constants	**Average Values (GPa)**	**% Error from DFT**
$\mathbf{C_{11}^{\dagger}}$	291.293	*±27.3%*
$\mathbf{C_{12}^{\dagger}}$	185.393	*±9.7%*
$\mathbf{C_{44}^{\dagger}}$	116.087	*±21.8%*

These results demonstrate a key trend: while uMLIP accurately reproduces equilibrium lattice geometry for pure Ni, it significantly underestimates stiffness components such as C_{11} and C_{44}. The relatively small error in C_{12} suggests partial reliability, but the broader discrepancies reinforce that uMLIP captures structural features more reliably than mechanical response—even in simple, single-element systems. This observation is consistent with deviations seen in multi-component alloys and highlights the need for improved force-field training with targeted emphasis on mechanical property fidelity.

Table 14: Pure Ni uMLIP Elastic Constant Data @ 300K

uMLIP Ni @ 300K	
Effective Elastic Constants	**Average Values (GPa)**
$\mathbf{C_{11}^{\dagger}}$	270.700
$\mathbf{C_{12}^{\dagger}}$	181.733
$\mathbf{C_{44}^{\dagger}}$	105.940

Elastic constant data for pure FCC Ni at 300 K were generated using the uMLIP model and are summarized in Table 14. Simulations were conducted using an 6,750-atom supercell. While DFT benchmark data exist for FCC Ni at 0 K, no equivalent reference values are currently available at 300 K. These results are included for completeness and trend observation but should be treated as exploratory until validated against finite-temperature DFT data or experimental measurements.

5.3 GSFE Comparison

This section evaluates the GSFE profiles predicted by the uMLIP model in comparison with DFT results, where available. The GSFE metric is critical for assessing dislocation mobility and intrinsic slip behavior in crystalline metals and alloys. Simulations were performed on key slip planes for each structure and composition at 0 K. DFT data were sourced from published literature and internal repositories for benchmarking purposes. Systems without DFT or

experimental GSFE data are discussed as exploratory predictions for future quantum-level validation.

5.3.1 CoNiRu: uMLIP vs DFT

To evaluate the accuracy of the uMLIP, results were compared against DFT data [65], which modeled dislocation core structures in equimolar CoNiRu multi-principal element alloys using ab initio-informed phase-field modeling. The DFT dataset included GSFE calculations across 90 distinct slip planes at 0 K. From this, the average GSFE for FCC CoNiRu was determined to be γ_{isf} = -44.56 $\frac{mJ}{m^2}$ and γ_{usf} = 376.41 $\frac{mJ}{m^2}$, with values ranging from -300 < γ_{isf} < 200$\frac{mJ}{m^2}$ and 200.

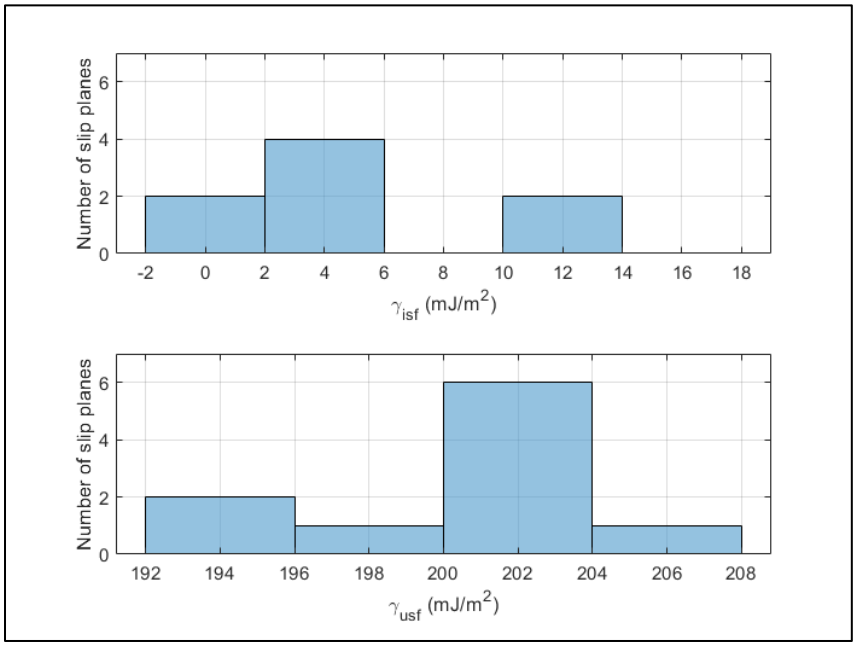

Figure 8: Distribution of γ_{isf} and γ_{usf} for FCC CoNiRu at 0 K

In comparison, uMLIP-based simulations were performed on 10 representative FCC slip planes at 0 K. The resulting GSFE curves displayed qualitative agreement with the DFT reference, exhibiting similar curve shapes and characteristic peak locations. The average stacking fault energies calculated using uMLIP were γ_{isf} = 5.92 $\frac{mJ}{m^2}$ and an average unstable stacking fault energy of γ_{usf} = 200.35 $\frac{mJ}{m^2}$, with ranges spanning -2 < γ_{isf} < 14 $\frac{mJ}{m^2}$ and 192 < γ_{usf} < 208 $\frac{mJ}{m^2}$. Although the uMLIP predictions are narrower in spread compared to the DFT dataset, it can

be observed that the average uMLIP GSFE calculations of 10 slip planes falls within the range of offered by the DFT calculations of 90 slip planes of FCC CoNiRu at 0K.

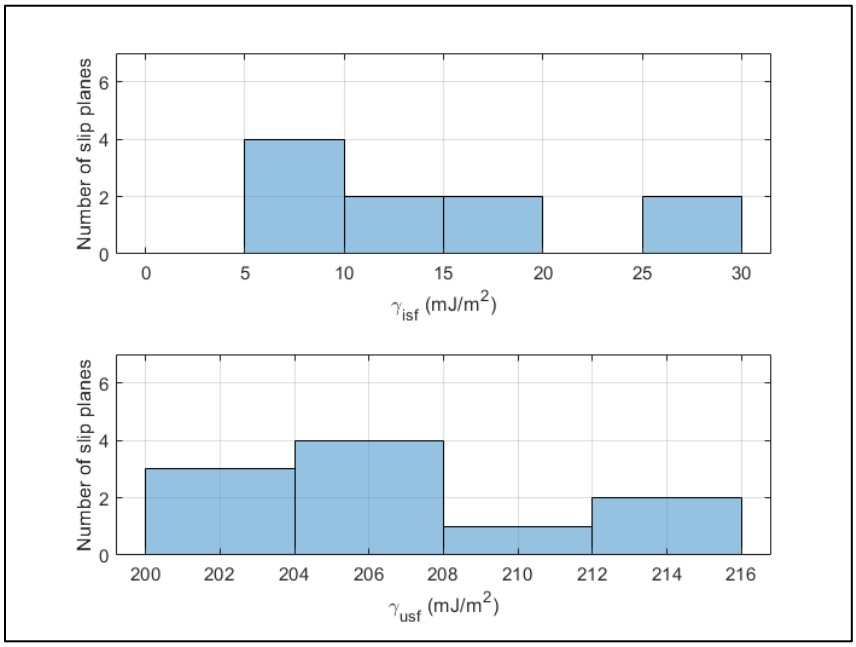

Figure 9: Distribution of γ_{isf} and γ_{usf} for HCP CoNiRu at 0 K

In addition to the FCC phase, GSFE calculations were also carried out using uMLIP for the HCP phase of CoNiRu at 0 K. Although no DFT reference currently exists for HCP CoNiRu, the computed values— γ_{isf} = 15.07 $\frac{mJ}{m^2}$ and γ_{usf} =207.50$\frac{mJ}{m^2}$ —exhibit trends consistent with typical HCP stacking fault behavior. These findings remain unvalidated and will require further benchmarking through DFT studies.

5.3.2 Co_2Ni_2Ru: uMLIP vs. DFT

For FCC Co_2Ni_2Ru at 0 K, unpublished DFT data reporting an average stacking fault energy of γ_{isf} = -43.11 $\frac{mJ}{m^2}$ was used as a benchmark to evaluate the performance of the uMLIP [58]. While the DFT values were not available across a wide range of slip systems, they served as a useful point of comparison. The uMLIP model was applied to 10 representative FCC slip planes at 0 K.

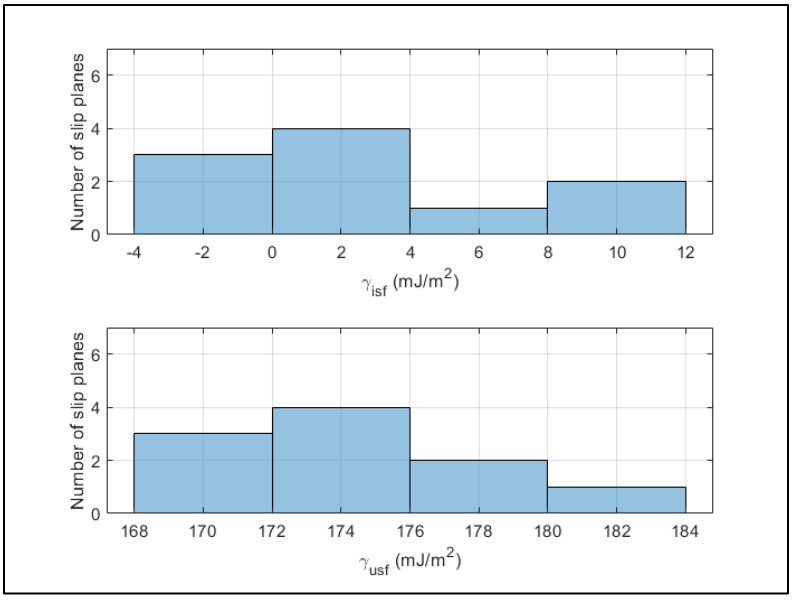

Figure 10: Histogram of FCC Co_2Ni_2Ru GSFE Values from uMLIP

From Figure 6, the GSFE curves produced by the model captured the correct order of magnitude for both intrinsic and unstable stacking fault energies, with average values of γ_{isf} = 3.23 $\frac{mJ}{m^2}$ and γ_{usf} = 174.17 $\frac{mJ}{m^2}$. The predicted energy ranges spanned from γ_{isf} = -4< x < 12 $\frac{mJ}{m^2}$ and γ_{usf} = 168 < x < 184 $\frac{mJ}{m^2}$. These profiles exhibited similar curve shapes to those expected from DFT, indicating that uMLIP effectively approximates the local energy gradients relevant to dislocation slip in FCC Co_2Ni_2Ru. However, it is noted that the DFT average γ_{isf} falls outside the range predicted by uMLIP, suggesting that while uMLIP captures qualitative trends, further tuning or training data may be needed for quantitative agreement in this specific composition.

5.3.3 $CoNiRu_2$: uMLIP Only

The average stacking fault energies predicted by uMLIP were γ_{isf} = 28.90 $\frac{mJ}{m^2}$ and γ_{usf} = 190.97 $\frac{mJ}{m^2}$, with respective ranges of 24 < γ_{isf} < 40 $\frac{mJ}{m^2}$ and 188 < γ_{usf} < 200 $\frac{mJ}{m^2}$.

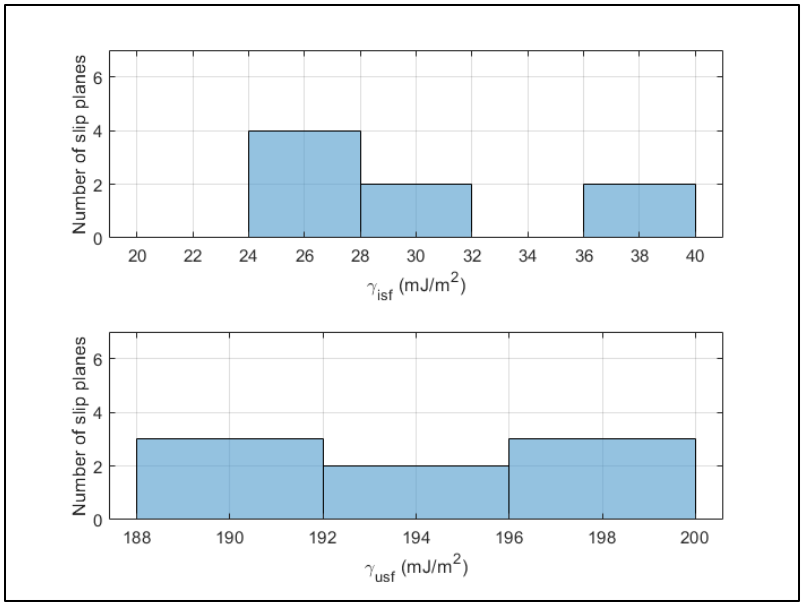

Figure 11: Histogram of HCP CoNiRu₂ GSFE Values from uMLIP at 0K

These values suggest a moderate intrinsic fault energy and a relatively low unstable stacking fault barrier, both of which fall within expected ranges for HCP alloy behavior.

As of May 2025, no DFT or experimental GSFE data has been published for $CoNiRu_2$, making direct benchmarking currently impossible. Despite this limitation, uMLIP simulations were performed on 10 representative slip planes in the HCP phase at 0 K to explore the alloy's stacking fault characteristics. The generated GSFE profiles exhibit features typical of HCP materials, including multiple local minima that are indicative of complex slip behavior in hexagonal systems. Although the results align qualitatively with known trends in hexagonal systems, their accuracy cannot yet be confirmed. Future quantum-level studies, such as DFT benchmarking, will be essential to validate the reliability of the uMLIP model for $CoNiRu_2$.

5.3.4 Pure Ni: uMLIP vs. DFT

Pure FCC Ni serves as a reliable reference system for GSFE benchmarking due to its well-defined slip planes and extensive quantum-mechanical data. According to published DFT findings for Pure Ni at 0K, the intrinsic stacking fault energy is γ_{isf} = 152.13 $\frac{mJ}{m^2}$ and the unstable stacking fault energy is γ_{usf} = 300.89 $\frac{mJ}{m^2}$ [64].

For Pure Ni, uMLIP simulations were performed on slip plane 5 at 0 K. The resulting GSFE curve retained the expected shape and energy barrier profile. The computed values were

γ_{isf} = 18.20 $\frac{mJ}{m^2}$ and γ_{usf} = 253.49 $\frac{mJ}{m^2}$, corresponding to percent errors of ±88.0% and ±15.8% or the intrinsic and unstable stacking fault energies, respectively. While the ISF energy was significantly underestimated, the USF value remained within a reasonable margin of error. These results demonstrate that uMLIP is capable of reproducing the qualitative GSFE landscape of pure FCC Ni. Despite some deviation in absolute values, particularly for γ_{isf}, the model shows reliable predictive behavior for single-element systems with clearly defined stacking sequences.

Chapter 6: Conclusions

6.1 Summary of Major Findings

This study conducted a comprehensive evaluation of the uMLIP using atomistic simulations of CoNiRu-based alloys across a range of compositions, crystal structures, and temperatures. The uMLIP model, implemented via the SevenNet neural network architecture and executed in LAMMPS, was assessed for its ability to predict key structural and mechanical properties—specifically lattice parameters, elastic constants, and GSFE.

The main findings are summarized as follows:

- **Lattice Parameter Predictions**:
  The uMLIP model demonstrated high accuracy in reproducing lattice parameters across all systems studied. For equiatomic CoNiRu (FCC), the predicted lattice parameter at 0 K was within **±0.7%** of the DFT reference. For Co_2Ni_2Ru, the uMLIP results at 0 K and 300 K were within **±2.3%** and **±3.0%** of the DFT and experimental values, respectively. Pure Ni also showed strong agreement within **±0.5%**, confirming the model's reliability in capturing volumetric properties.

  Notably, the lattice parameters were **consistently larger at 300 K than at 0 K** across all systems where both temperatures were evaluated. This outcome aligns with physical expectations due to **thermal expansion**: as temperature increases, atoms vibrate with greater amplitude and require more space, leading to an increase in average interatomic distances. This temperature-induced expansion is a well-documented behavior in crystalline solids and serves as an additional validation point for the thermodynamic realism of the uMLIP model.

- **Elastic Constant Predictions**:
  Elastic constants predicted by uMLIP showed significant deviations from DFT values across nearly all systems. For CoNiRu and Co_2Ni_2Ru (FCC, 0 K), uMLIP failed to consistently reproduce stiffness trends, and no significant improvement was observed at 300 K. Even for pure Ni, the uMLIP showed notable error compared to established DFT values. These results suggest that while the model captures geometric equilibrium well, it struggles to resolve force-based second-order properties.

  When comparing elastic constants between 0 K and 300 K, the predicted stiffness values from uMLIP were generally **lower at 300 K**, which is also physically consistent. As temperature increases, atomic vibrations increase, reducing resistance to deformation and softening the material. This thermal softening effect is expected in most metallic systems and reinforces that, while uMLIP may lack quantitative precision, it qualitatively captures correct thermomechanical trends.

- **GSFE Profiles**:
  The uMLIP model produced GSFE curves for FCC CoNiRu that fell within the range of DFT-calculated profiles across multiple slip systems. Although uMLIP used only 10 slip planes compared to 90 in the DFT reference, it successfully replicated the qualitative features of the energy-displacement curve. For Co_2Ni_2Ru and pure Ni, GSFE predictions were also reasonable, supporting the model's effectiveness in approximating deformation behavior. GSFE results for $CoNiRu_2$ (HCP) and other unbenchmarked systems remain exploratory.

- **General Assessment of uMLIP**:
  The uMLIP (SevenNet + LAMMPS) framework is a promising tool for large-scale simulations of complex alloy systems, capable of delivering accurate lattice predictions at significantly reduced computational cost compared to DFT. However, its current formulation lacks the precision needed for elastic property prediction, especially in multi-principal element alloys with chemical disorder.

These findings reinforce the potential of universal MLIPs as efficient approximators for structural properties but highlight the need for further development and validation—particularly in the context of mechanical property prediction. The model's ability to reproduce physically

expected trends in thermal expansion and elastic softening is encouraging, but quantitative consistency remains a key challenge.

6.2 Accuracy and Limitations of uMLIP

The uMLIP used in this study, based on the SevenNet architecture, displayed varying levels of accuracy depending on the class of material properties evaluated. While it proved effective in predicting equilibrium lattice parameters across diverse CoNiRu alloy compositions and structures, it exhibited notable shortcomings when tasked with replicating mechanical stiffness and deformation behavior.

Strengths of uMLIP:

- Demonstrated high fidelity in predicting **lattice parameters** for all tested systems, with deviations typically under ±3% when compared to DFT or experimental references.
- Successfully approximated GSFE trends in FCC CoNiRu and Co_2Ni_2Ru systems, producing energy curves with comparable features to DFT.
- Enabled simulation of large atomic systems (>20,000 atoms), offering scalability unattainable by DFT.

Limitations of uMLIP:

- Failed to consistently predict elastic constants, with high and erratic error margins across C_{11}, C_{12}, and C_{44} components.
- Elastic constant deviations were evident not only in chemically complex systems (e.g., CoNiRu, Co_2Ni_2Ru) but also in simpler systems like pure Ni.
- **Temperature effects** on elasticity were poorly captured, indicating a limited sensitivity to thermodynamic variations.
- GSFE agreement, while qualitatively reasonable, was only benchmarked at **0 K**; thermal effects on dislocation behavior remain unverified.

In summary, the uMLIP is a strong candidate for approximating structural equilibrium states in multi-component alloys but lacks the precision required for high-confidence mechanical property

predictions. These findings suggest that further training or model refinement may be necessary for force-sensitive applications such as elasticity and phonon modeling.

6.3 Future Work and Recommendations

While these benchmarks provides a foundational assessment of the uMLIP for CoNiRu-based alloys, several opportunities for future work remain—particularly in addressing the limitations observed in property prediction and benchmarking accuracy. The next steps should focus on both improving the quality and breadth of reference data, and strategically probing areas where uMLIP performance can be better validated or extended.

The most immediate need is for additional DFT calculations to benchmark the uMLIP across a wider set of structural and mechanical properties. While DFT comparisons were possible for lattice parameters in most systems, elastic constants and GSFE data were limited or unavailable for several key compositions, particularly at elevated temperatures and in HCP phases. Targets for DFT benchmarking missing from this study include:

- Elastic constants for $CoNiRu_2$ (HCP) and Co_2Ni_2Ru (FCC) at 300 K
- GSFE curves in HCP CoNiRu and $CoNiRu_2$
- Temperature-dependent DFT simulations to compare with uMLIP-predicted thermal trends

By having accurate data for these benchmarking sets, the limitations of the current uMLIP model can more confidently be assessed and improve reliability of model-driven alloy design.

Complex alloys also exhibit local phenomena such as chemical short-range ordering (CSRO) and local slip resistance (LSR), both of which can strongly influence mechanical behavior at the atomic scale. These effects introduce anisotropies and local environment dependencies that are often lost in randomly initialized atomistic models. At present, the uMLIP framework does not explicitly account for CSRO or LSR, which may contribute to its limited accuracy in elastic constant predictions. Future studies should explore the role of local ordering by simulating both ordered and disordered configurations of the same composition, comparing their predicted mechanical properties, and identifying whether the model is sensitive to such variations. Data augmentation strategies, including representative CSRO structures or LSR-

relevant configurations in the training or validation sets, may improve the model's ability to capture atomic-level mechanical phenomena.

Similarly, while this study utilized 10 representative slip planes for each GSFE calculation, reference DFT datasets often include 60–90 slip systems to fully characterize the anisotropic deformation behavior of complex alloys. An important next step is to expand the number of slip planes evaluated using uMLIP—particularly in FCC and HCP systems, where direction-dependent GSFE behavior plays a critical role in dislocation motion and deformation mechanics. Future work should simulate full GSFE surfaces with denser slip sampling in all major crystallographic directions. This would allow a more thorough evaluation of how well uMLIP captures fault energy variation across complex slip paths. Additionally, retraining or fine-tuning the model using DFT-calculated GSFE datasets may improve its performance in deformation-related predictions and strengthen its integration with dislocation or crystal plasticity models.

Finally, to build greater confidence in the predictive utility of MLIPs, future simulations should be designed to align with experimental observations or to support multi-scale modeling workflows. For instance, lattice parameter predictions at 300 K could be directly compared to available X-ray diffraction measurements. uMLIP-derived elastic constants and GSFE values could also be incorporated into phase-field models or finite element simulations to study macroscopic properties such as creep, fatigue resistance, or high-temperature deformation. These comparative approaches would not only validate the atomistic predictions but also demonstrate the broader utility of uMLIP in practical alloy design and performance modeling.

References

[1] J. Konrad and D. Zahn, "Assessing the mechanical properties of molecular materials from atomic simulation," AIMS Materials Science, vol. 8, no. 6, pp. 867–880, Dec. 2021.

[2] NASA Technology Transfer Program, "NASA Technology Brings the Heat with New Alloys and Ablators," Jan. 25, 2022.

[3] Y. Zhang et al., "Lignin-assisted alloying engineering of CoNiRu trimetallic nano-catalyst for effective overall water splitting," Journal of Alloys and Compounds, vol. 924, p. 166620, Jan. 2022.

[4] Y. Zhang and D. G. Truhlar, "Density Functional Theory for Transition Metals and Transition Metal Chemistry," Journal of Chemical Physics, vol. 130, no. 23, p. 234111, Jun. 2009.

[5] P. Verma and D. G. Truhlar, "Status and Challenges of Density Functional Theory," Trends in Chemistry, vol. 2, no. 4, pp. 302–318, Apr. 2020.

[6] M. S. Daw and M. I. Baskes, "Embedded-atom method: Derivation and application to impurities, surfaces, and other defects in metals," Physical Review B, vol. 29, no. 12, pp. 6443–6453, Jun. 1984.

[7] M. I. Baskes, "Modified embedded-atom potentials for cubic materials and impurities," Physical Review B, vol. 46, no. 5, pp. 2727–2742, Aug. 1992.

[8] E. J. Weiss et al., "Rapid Production of Accurate Embedded-Atom Method Potentials for Metal Alloys," arXiv preprint arXiv:2208.02223, Aug. 2022.

[9] W. A. Curtin, S. I. Rao, and C. Woodward, "Progress and challenges in the theory and modeling of complex concentrated alloys," MRS Bulletin, vol. 47, no. 2, pp. 109–116, Feb. 2022.

[10] X. Liu, J. Zhang, and Z. Pei, "Machine Learning for High-entropy Alloys: Progress, Challenges and Opportunities," arXiv preprint arXiv:2209.03173, Sep. 2022.

[11] L. Jiang et al., "A rapid and effective method for alloy materials design via sample data transfer machine learning," npj Computational Materials, vol. 9, no. 26, Feb. 2023.

[12] H. Sun et al., "A Knowledge Transfer Framework for General Alloy Materials Properties Prediction," Materials, vol. 15, no. 20, p. 7139, Oct. 2022.

[13] Q.-J. Li, H. Sheng, and E. Ma, "Strengthening in multi-principal element alloys with local-chemical-order roughened dislocation pathways," Nature Communications, vol. 10, no. 3563, Aug. 2019.

[14] S. Mubassira, W.-R. Jian, and S. Xu, "Effects of Chemical Short-Range Order and Temperature on Basic Structure Parameters and Stacking Fault Energies in Multi-Principal Element Alloys," Modelling, vol. 5, no. 1, pp. 352–366, Jan. 2024.

[15] M. Yamakata et al., "High pressure synthesis of a hexagonal close-packed phase of the high-entropy alloy CrMnFeCoNi," Nature Communications, vol. 8, no. 15634, Jun. 2017.

[16] Y. Mishin, “Machine-learning interatomic potentials for materials science,” arXiv preprint arXiv:2102.06163, Feb. 2021.

[17] E. J. Weiss et al., “General-purpose machine-learned potential for 16 elemental metals and their alloys,” Nature Communications, 2024.

[18] N. Leimeroth, L. C. Erhard, K. Albe, and J. Rohrer, “Machine-l earning interatomic potentials from a users perspective: A comparison of accuracy, speed and data efficiency,” arXiv preprint arXiv:2505.02503, May 2025.

[19] Erhard L.C., et al., “Cartesian atomic moment machine learning interatomic potentials,” npj Computational Materials, vol. X, Art. no. Y, May 2025.

[20] J. M. Haile, “Molecular Dynamics Simulation: Elementary Methods,” Wiley-Interscience, 1992.

[21] J. A. Anderson and S. C. Glotzer, "How do molecular dynamics simulations scale with time and system size?", ACS Nano, vol. 14, no. 2, pp. 1483–1490, 2020.

[22] Q. Ke et al., "Effects of Thermostats/Barostats on Physical Properties of Liquids by Molecular Dynamics Simulations," Journal of Molecular Liquids, vol. 365, p. 120116, Aug. 2022.

[23] Molecular Statics – an overview, ScienceDirect Topics.

[24] V. Riedl and J. K. N. Lindner, “Applicability of molecular statics simulation to partial dislocations in GaAs,” arXiv preprint arXiv:1909.09013, Sep. 2019.

[25] W. Kohn and L. J. Sham, “Self-consistent equations including exchange and correlation effects,” Physical Review, vol. 140, no. 4A, pp. A1133–A1138, Nov. 1965.

[26] P. Hohenberg and W. Kohn, “Inhomogeneous electron gas,” Physical Review, vol. 136, no. 3B, pp. B864–B871, Nov. 1964.

[27] “Kohn–Sham equations,” Wikipedia (accessed June 2025).

[28] J. Hafner, "Ab-initio simulations of materials using VASP: Density-functional theory and beyond," Journal of Computational Chemistry, vol. 29, no. 13, pp. 2044–2078, Oct. 2008.

[29] L. Fiedler, K. Shah, M. Bussmann, and A. Cangi, “A deep dive into machine learning density functional theory for materials science and chemistry,” arXiv preprint arXiv:2110.00997, Oct. 2021.

[30] P. Verma and D. G. Truhlar, "Status and challenges of density functional theory," Trends in Chemistry, vol. 2, no. 4, pp. 302–318, Apr. 2020.

[31] Y. Liu, X. He, and Y. Mo, “Discrepancies and error evaluation metrics for machine learning interatomic potentials,” npj Computational Materials, vol. 9, Art. 174, Nov. 2023.

[32] N. Leimeroth, L. C. Erhard, K. Albe, and J. Rohrer, “Machine-learning interatomic potentials from a users perspective: A comparison of accuracy, speed and data efficiency,” arXiv preprint arXiv:2505.02503, May 2025.

[33] M. H. Muser, S. V. Sukhomlinov, and L. Pastewka, “Interatomic potentials: Achievements and challenges,” Materials Theory, vol. 6, no. 1, pp. 1–26, Apr. 2022.

[34] M. A. Wood, M. A. Cusentino, B. D. Wirth, and A. P. Thompson, “Data-driven material models for atomistic simulation,” Physical Review B, vol. 99, p. 184305, May 2019.

[35] J. E. Lennard-Jones, “On the determination of molecular fields. II. From the equation of state of a gas,” Proceedings of the Royal Society A, vol. 106, no. 738, pp. 463–477, Jan. 1925.

[36] P. Schwerdtfeger, A. Burrows, and O. R. Smits, “The Lennard-Jones potential revisited—analytical expressions for vibrational effects in cubic and hexagonal close-packed lattices,” Ann. Phys., vol. 532, no. 9, p. 2000254, 2020.

[37] G. Rutkai, M. Thol, R. Span, and J. Vrabec, “How well does the Lennard-Jones potential represent the thermodynamic properties of noble gases?” J. Chem. Phys., vol. 147, no. 17, p. 174504, Nov. 2017.

[38] M. S. Daw and M. I. Baskes, “Embedded-atom method: Derivation and application to impurities, surfaces, and other defects in metals,” Physical Review B, vol. 29, no. 12, pp. 6443–6453, Jun. 1984.

[39] A. F. Voter and S. P. Chen, “Accurate interatomic potentials for Ni, Al, and Ni3Al,” Materials Research Society Symposium Proceedings, vol. 82, pp. 175–180, 1987.

[40] Y. Mishin et al., “Structural stability and lattice defects in copper: Ab initio, tight-binding, and embedded-atom calculations,” Physical Review B, vol. 63, no. 22, p. 224106, May 2001.

[41] M. I. Baskes, “Modified embedded-atom potentials for cubic materials and impurities,” Physical Review B, vol. 46, no. 5, pp. 2727–2742, Aug. 1992.

[42] R. J. Jiang, H. J. Liu, Y. Q. Wang, and L. Q. Chen, “A modified embedded-atom method potential for a quaternary Fe–Cr–Si–Mo alloy,” Materials, vol. 16, no. 7, p. 2825, Apr. 2022.

[43] M. I. Baskes, “Modified embedded-atom potentials for cubic materials and impurities,” Physical Review B, vol. 46, no. 5, pp. 2727–2742, Aug. 1992.

[44] J. Houze et al., “A multi-objective optimization procedure to develop modified-embedded-atom-method potentials: an application to magnesium,” arXiv preprint arXiv:0708.0075, Aug. 2007.

[45] J. Tersoff, “New empirical model for the structural properties of silicon,” Physical Review Letters, vol. 56, no. 6, pp. 632–635, Feb. 1986; further developed in “New empirical approach for the structure and energy of covalent systems,” Physical Review B, vol. 37, no. 12, pp. 6991–7000, May 1988.

[46] F. H. Stillinger and T. A. Weber, “Computer simulation of local order in condensed phases of silicon,” Physical Review B, vol. 31, no. 8, pp. 5262–5271, Apr. 1985.

[47] S. M. Rassoulinejad-Mousavi and Y. Zhang, “Interatomic Potentials Transferability for Molecular Simulations: A Comparative Study for Platinum, Gold and Silver,” Scientific Reports, vol. 8, no. 2424, 2018.

[48] M. A. Wood, M. A. Cusentino, B. D. Wirth, and A. P. Thompson, “Data-driven material models for atomistic simulation,” Physical Review B, vol. 99, p. 184305, May 2019.

[49] J. M. Verstraelen and M. K. Choi, “Machine learning interatomic potentials from a user’s perspective: A comparison of accuracy, speed and data efficiency,” arXiv preprint arXiv:2505.02503, May 2025.

[50] M. R. K. M. Tok and D. W. Jacobs, “Atomistic modeling of the mechanical properties: the rise of machine learning interatomic potentials,” Materials Horizons, vol. 10, no. 5, pp. 1203–1225, 2023.

[51] Z. Zhang et al., “General-purpose machine-learned potential for 16 elemental metals and their alloys,” Nature Communications, vol. 15, Art. 10208, 2024.

[52] M. Park, J. Kim, S. Hwang, and S. Han, “Scalable parallel algorithm for graph neural network interatomic potentials in molecular dynamics simulations,” Journal of Chemical Theory and Computation, vol. 20, no. 11, pp. 4857–4868, 2024.

[53] Y. Park, J. Kim, S. Hwang, and S. Han, “Scalable parallel algorithm for graph neural network interatomic potentials in molecular dynamics simulations,” Journal of Chemical Theory and Computation, vol. 20, no. 11, pp. 4857–4868, Nov. 2024.

[54] S. J. Plimpton, “Fast parallel algorithms for short-range molecular dynamics,” Journal of Computational Physics, vol. 117, no. 1, pp. 1–19, Mar. 1995; S. Gravelle, J. Gissinger, and A. Kohlmeyer, “A set of tutorials for the LAMMPS simulation package,” LiveCoMS, Mar. 2025.

[55] M.-A. Charpagne et al., "Design of Nickel-Cobalt-Ruthenium Multi-Principal Element Alloys," Acta Materialia, vol. 194, pp. 160–173, Aug. 2020.

[56] A. W. Hull, "X-Ray Crystal Analysis of Thirteen Common Metals," Physical Review, vol. 17, no. 5, pp. 571–588, May 1921.

[57] M. Wang, Y. Zeng, Y. Chen, S. Zhang, and X. Wang, “Crystal structure effect on metallic mechanical properties under tension stress: Molecular dynamics study,” Proceedings of the Engineering for Rural Development Conference, Jelgava, Latvia, May 2023.

[58] S. Xu, “CoNiRu_2025: Atomistic Simulations of CoNiRu Alloys,” GitHub repository, 2025. [Online].

[59] “LAMMPS Tube, Lattice Parameter Calculation,” Unnamed Blog & Tutorial, Nov. 14, 2019.

[60] S. J. Plimpton, “Fast parallel algorithms for short-range molecular dynamics,” Journal of Computational Physics, vol. 117, no. 1, pp. 1–19, Mar. 1995.

[61] J. Wang and A. Misra, "An overview of interface-dominated deformation mechanisms in metallic multilayers," Current Opinion in Solid State and Materials Science, vol. 15, no. 1, pp. 20–28, 2011.

[62] S. Plimpton, A. Thompson, and P. Crozier, “LAMMPS: A flexible simulation tool for particle-based materials modeling at the atomic, meso, and continuum scales,” Modelling and Simulation in Materials Science and Engineering, vol. 27, no. 7, p. 073001, 2019.

[63] M. A. Charpagne, K. V. Vamsi, Y. M. Eggeler, S. P. Murray, C. Frey, S. K. Kolli, and T. M. Pollock, "Design of Nickel-Cobalt-Ruthenium Multi-Principal Element Alloys," *Acta Materialia*, vol. 194, pp. 224–235, Aug. 2020.

[64] S. Xu, M. A. Tschopp, and I. J. Beyerlein, "Density functional theory calculations of stacking fault energies in CoNiRu multi-principal element alloys," *J. Appl. Phys.*, vol. 126, no. 10, p. 105112, Sep. 2019.

[65] Y. Su, S. Xu, and I. J. Beyerlein, "Ab initio-informed phase-field modeling of dislocation core structures in equal-molar CoNiRu multi-principal element alloys," *Modelling Simul. Mater. Sci. Eng.*, vol. 27, no. 8, p. 085010, Aug. 2019.